Figures and figure supplements

Structural and regulatory insights into the glideosome-associated connector from *Toxoplasma gondii*

Amit Kumar *et al*.

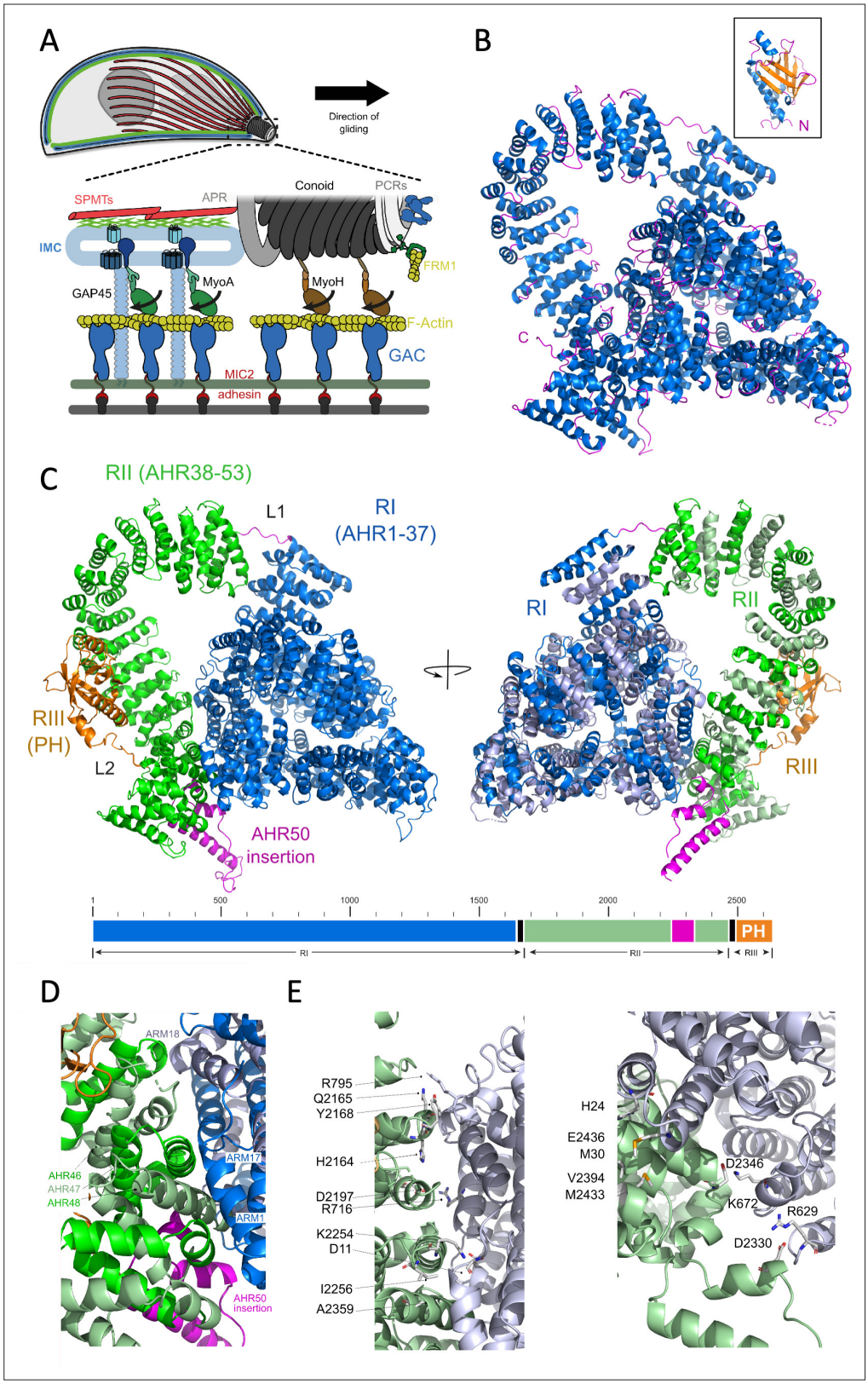

Figure 1. The organisation and structure of TgGAC. (**A**) Schematic diagram of the apicomplexan glideosome. Key molecular components and structures are indicated, including subpellicular microtubules (SPMTs), inner membrane complex (IMC), preconoidal rings (PCRs), apical polar ring (APR), Formin-1 (FRM1), filamentous actin (F-actin), glideosome-associated protein 45 (GAP45), myosin motors (MyoA and MyoA), microneme protein 2 (MIC2), and

Figure 1 continued on next page

Figure 1 continued

glideosome-associated connector (GAC) protein. (**B**) Crystal structure of $TgGAC_{7–2504}$ and representative nuclear magnetic resonance (NMR) model of $TgGAC_{2505–2639}$ (inset). Helices shown in blue, β-strands in orange and loops in magenta. (**C**) Full-length TgGAC model comprising the combined crystal structure and NMR-validated AlphaFold2 structures in (**B**). Region I (R1: residues 1–1665) comprising the first 37 consecutive armadillo (ARM)/HEAT-like repeats (AHRs) is supercoiled into a three-layer pyramid structure (blue). AHR region II comprising 16 ARM repeats (RII: AHR38-53 residues 1670–2489) forms the superhelical arch (green). The C-terminal PH domain encompassing 2511–2639 of RIII is shown in orange (left). Second orientation related by a 180° rotation with even numbered AHRs shown in grey and odd number shown in blue for RI and green for RII. The R1–RII linker and AHR50 which has a helix-loop-helix insertion are shown in magenta. (**D**) The N/C interface between RI and RII showing key interacting AHRs. (**E**) Key residues specific interactions across the N/C interface. Cartoon representations coloured in light blue for RI and light green for RII.

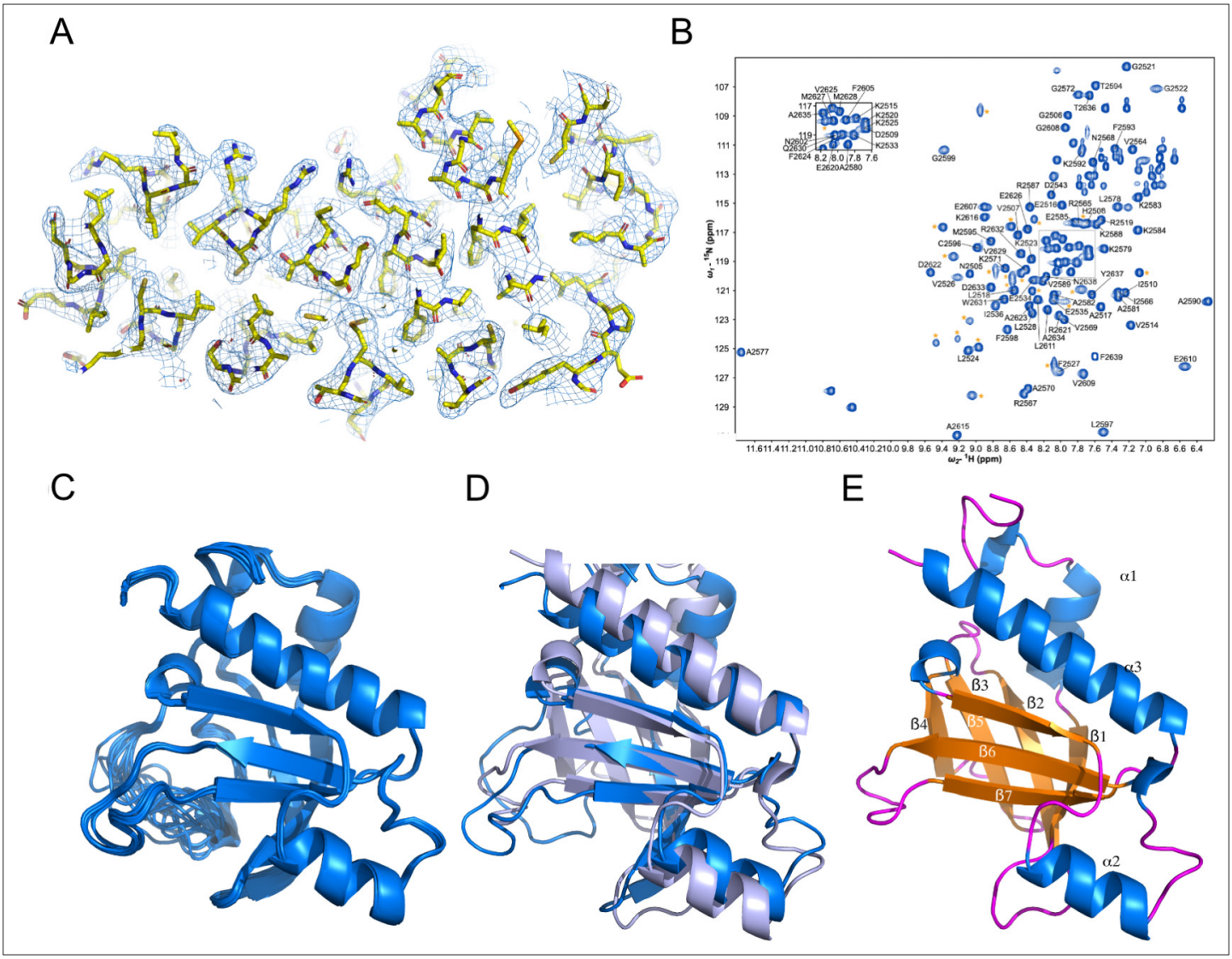

Figure 1—figure supplement 1. Assessing the quality of structural data for glideosome-associated connector (GAC). (**A**) Representative X-ray crystallographic electron density map showing the fit to residues 1203–1453 from the final model. (**B**) Assigned ^{1}H-^{15}N HSQC nuclear magnetic resonance (NMR) spectrum for $TgGAC_{PH}$ ($TgGAC_{2505–2639}$). (**C**) Superposition of the the 20 low energy structure of $TgGAC_{PH}$ from the NMR ensemble. (**D**) Superposition of the Alphafold2 structure of $TgGAC_{PH}$ with a representative NMR structure. (**E**) Structural $TgGAC_{PH}$ coloured according to annotated secondary structure.

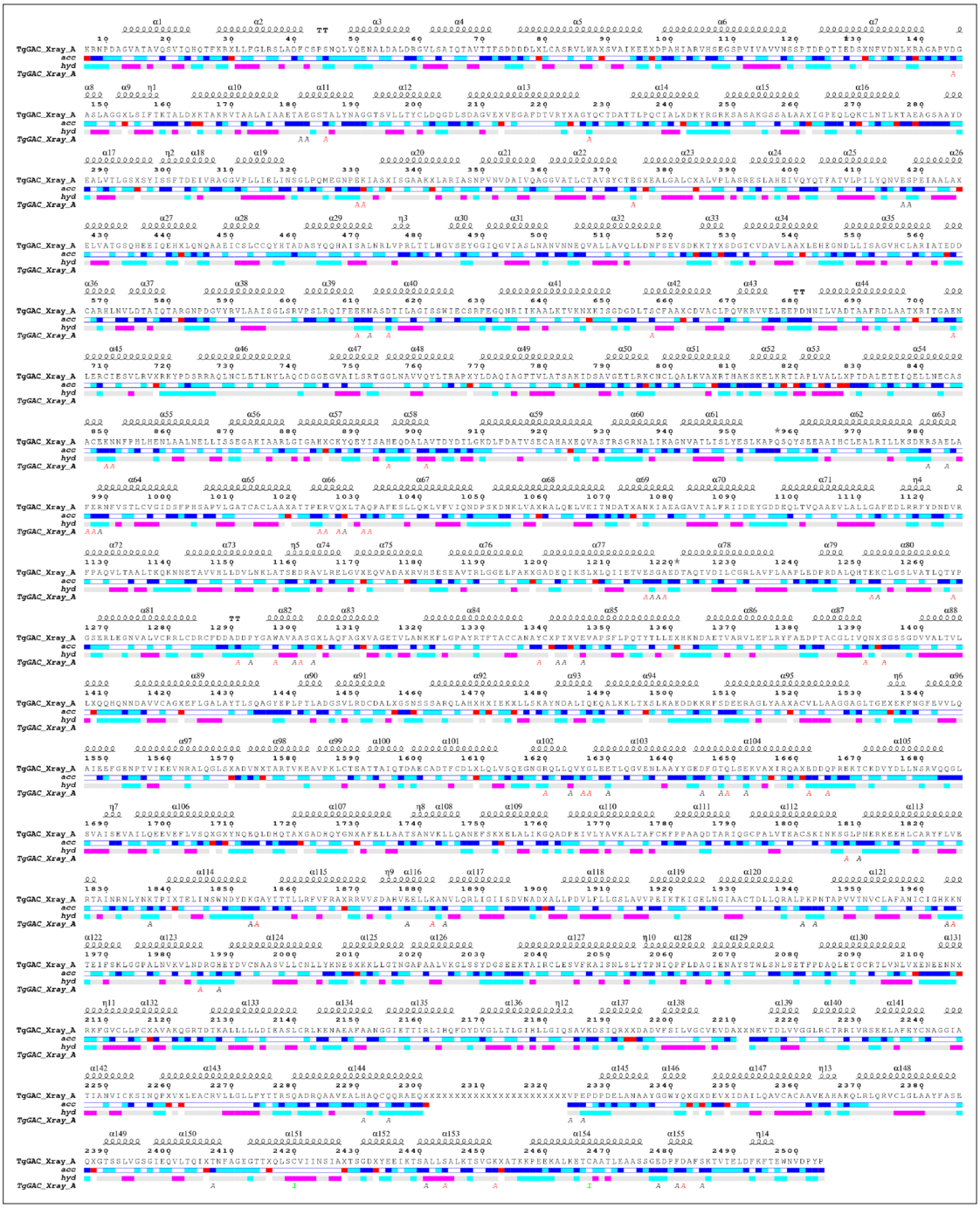

Figure 1—figure supplement 2. Secondary structure for the crystal structure of TgGAC. Representation generated using ENDscript (***Robert and Gouet, 2014***). α-helices labelled α1, α2…, and α156, other helix types η 1, η 2…, and β-strands by their sheets β1… β7 and turn with TT.

Figure 1—figure supplement 3. Structural homology with TgGAC. Comparisons of the structure of the C-terminal armadillo (ARM)-rich arch of TgGAC with human p120 catenin/E-cadherin (PDB 3L6X), β-catenin//E-cadherin from *Caenorhabditis elegans* (PDB 4R10), human plakoglobin/E-cadherin (PDB 3IFQ) and UNC45 myosin chaperone *Caenorhabditis elegans* (PDB 6QDL). Orientations are chosen by superposing over equivalent ARMs.

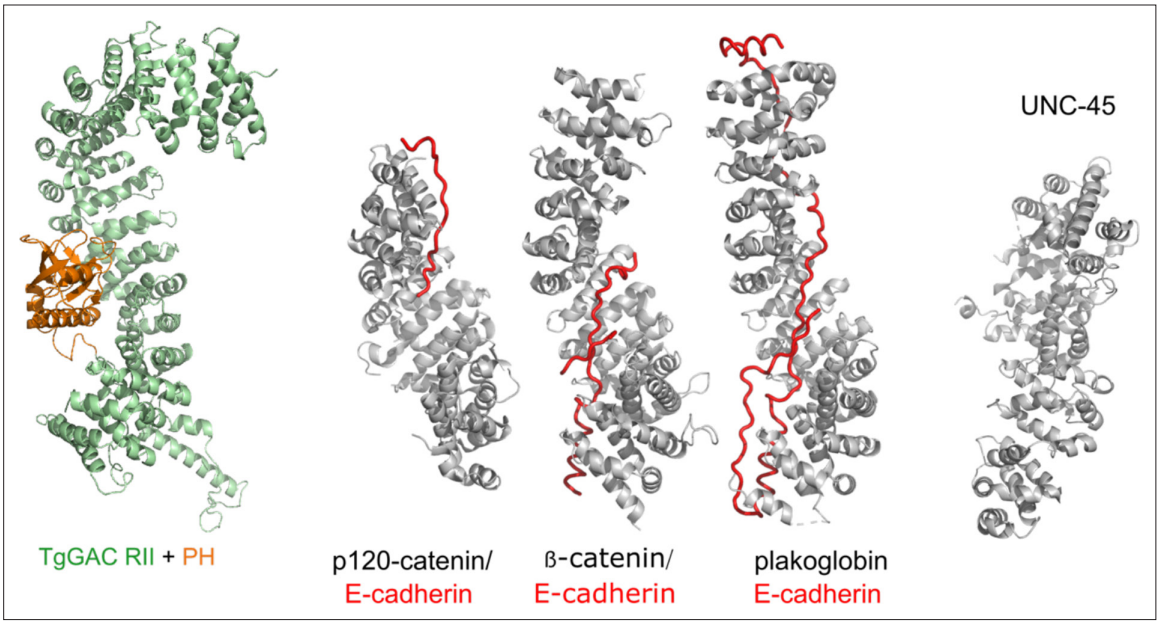

Figure 1—figure supplement 4. Sequence alignment for the crystal structure of TgGAC. Sequence alignment of selected glideosome-associated connector (GAC) homologues with domain architecture and key interface, phosphatidic acid (PA) binding residues indicated.

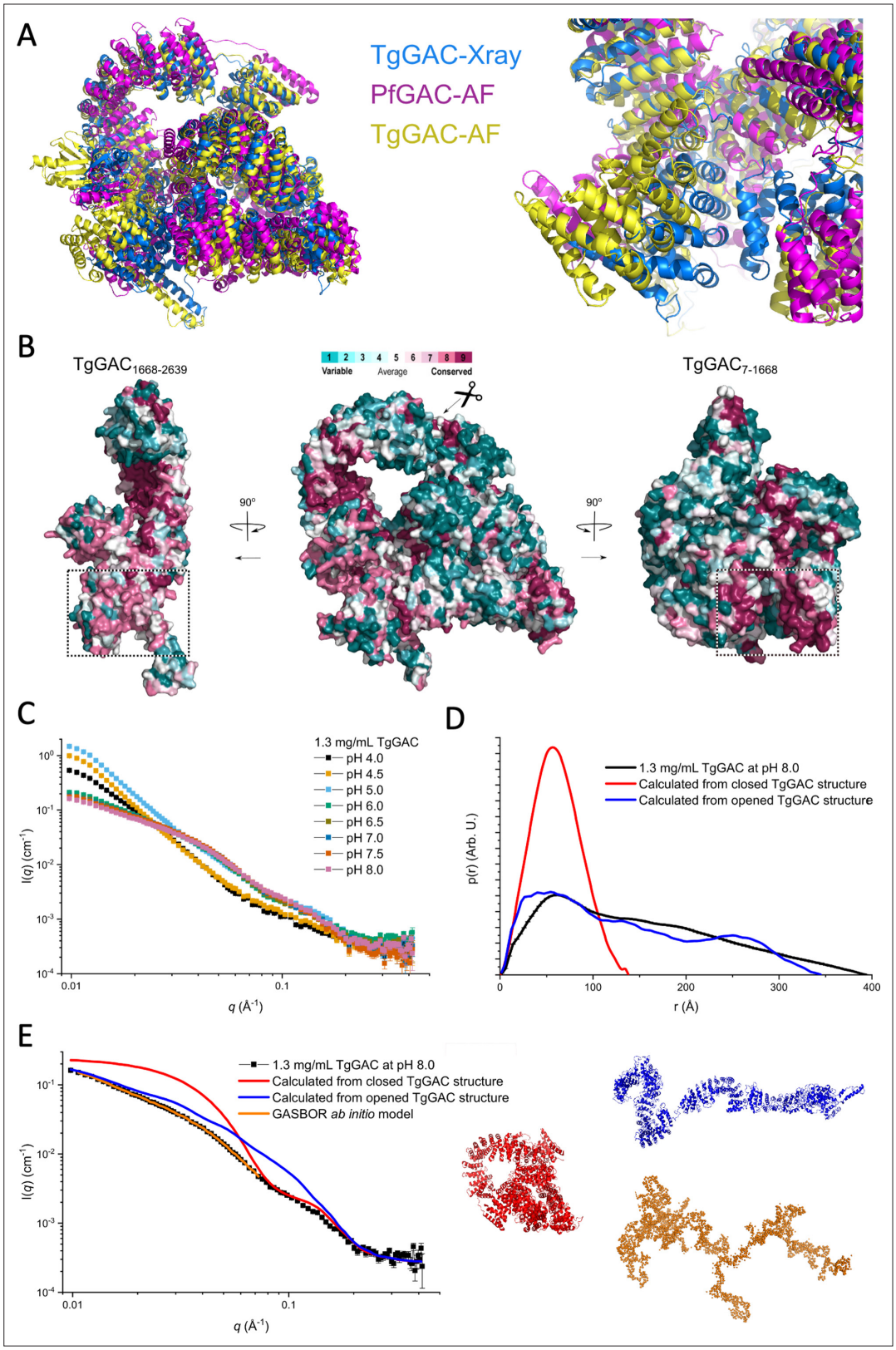

Figure 2. Glideosome-associated connector (GAC) adopts both open and closed structures. (**A**) Superimposition of the experimentally determined composite structure of TgGAC with those generated from AlphaFold2 for TgGAC and PfGAC, showing that the closed structure is conserved (left). N/C-terminal interface is highly similar but partially opened in the predicted structures of TgGAC and PfGAC. The PH domain is not displayed for clarity

Figure 2 continued on next page

Figure 2 continued

(right). (**B**) Conservation profile on a surface representation for TgGAC in three different orientation generated using ConSurf (***Landau et al., 2005***). Centre – full-length TgGAC in the same conformation as (**A**). TgGAC is split in two and each half rotated 90° to display the N/C interface. C-terminal regions RII and RIII (left) and N-terminal region RI (right). The surface is coloured according to its ConSurf conservation score, which varies from cyan which are highly variable to maroon for highly conserved. (**C**) Small-angle X-ray scattering (SAXS) data for GAC at pH 4.0–8.0. (**D**) Pair distance distribution functions (*p(r)*) for GAC SAXS data at pH 8.0, calculated from full-length closed TgGAC structure and calculated for the opened structure generated by molecular dynamic (MD) simulations. (**E**) Modelling of TgGAC solution structure at pH 8.0, calculated theoretical scattering curves for the full-length closed TgGAC structure (red), and calculated for the opened full-length TgGAC structure (blue), and a GASBOR *ab initio* model (orange). Structures are shown in colours corresponding to those of the scattering curves.

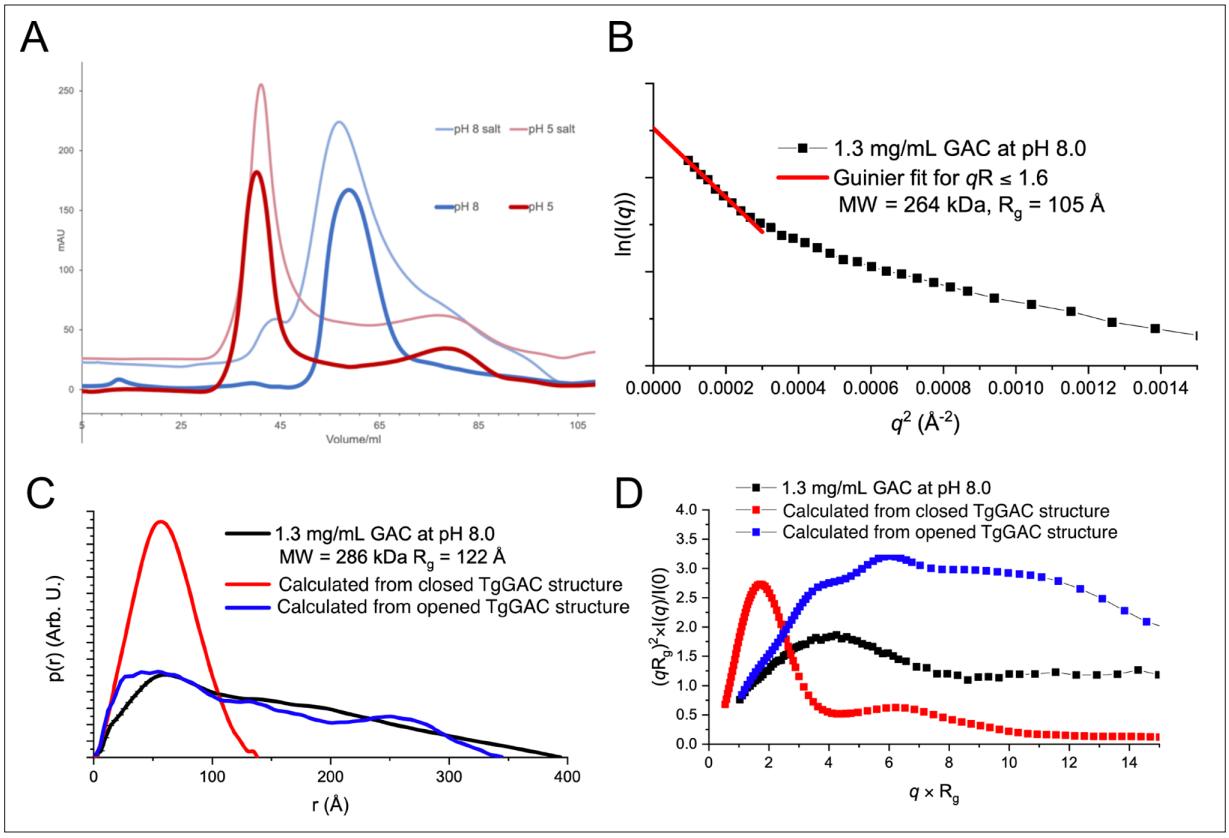

Figure 2—figure supplement 1. Size-exclusion chromatography of glideosome-associated connector (GAC) and analysis of small-angle X-ray scattering (SAXS) data at pH 8.0 with comparison to crystal structure. (**A**) Size exclusion chromatography (SEC) profiles for 4 mg/ml TgGAC at pH 5 (25 mM sodium acetate) and pH 8 (25 mM Tris) in the presence and absence of 100 mM NaCl. (**B**) Guinier fit of TgGAC SAXS data using the first eight points. The molecular mass (MW) and radius of gyration (Rg) calculated from the Guinier fit are noted in the legend. (**C**) *p(r)* functions for TgGAC SAXS data (black), the full length closed TgGAC structure (red), and the molecular dynamics generated opened TgGAC structure (blue). The MW and Rg calculated from indirect Fourier transform (IFT) routine for SAXS data are noted in the legend. (**D**) Dimensionless Kratky plot for TgGAC SAXS data (black), the full length closed TgGAC structure (red), and the molecular dynamics generated opened TgGAC structure (blue).

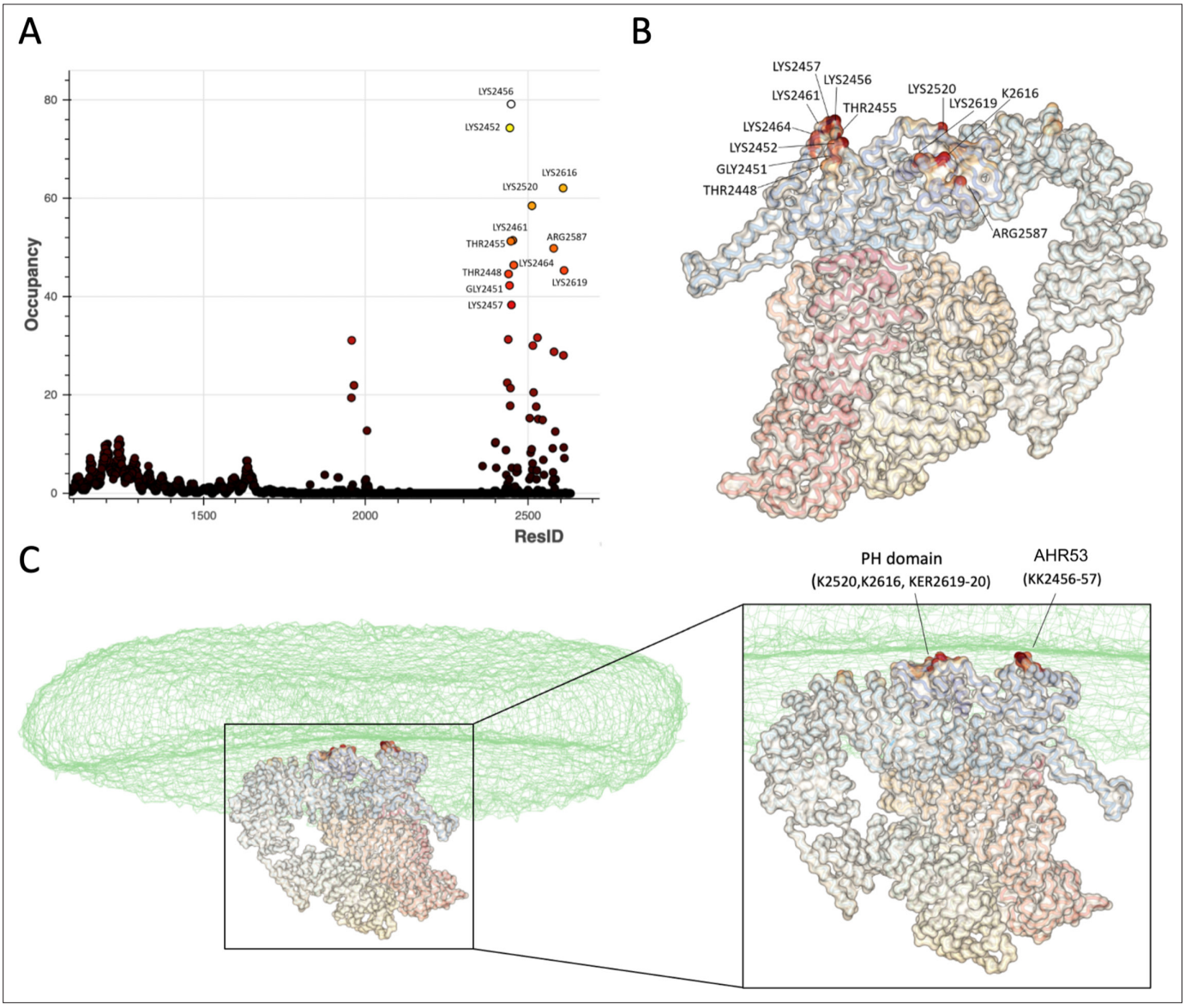

Figure 3. Simulation of TgGAC binding to phosphatidic acid (PA)-containing membranes. (**A**) Analysis of residues that interact with 1-palmitoyl-2-oleoyl-sn-glycero-3-phosphate (POPA) as a percentage of contact during the simulation time. Analysis was performed for the final 5 μs of the simulation. (**B**) Key residues from mapped onto the TgGAC structure. (**C**) As in (**B**) in the contact of the membrane which is displayed as a transparent surface.

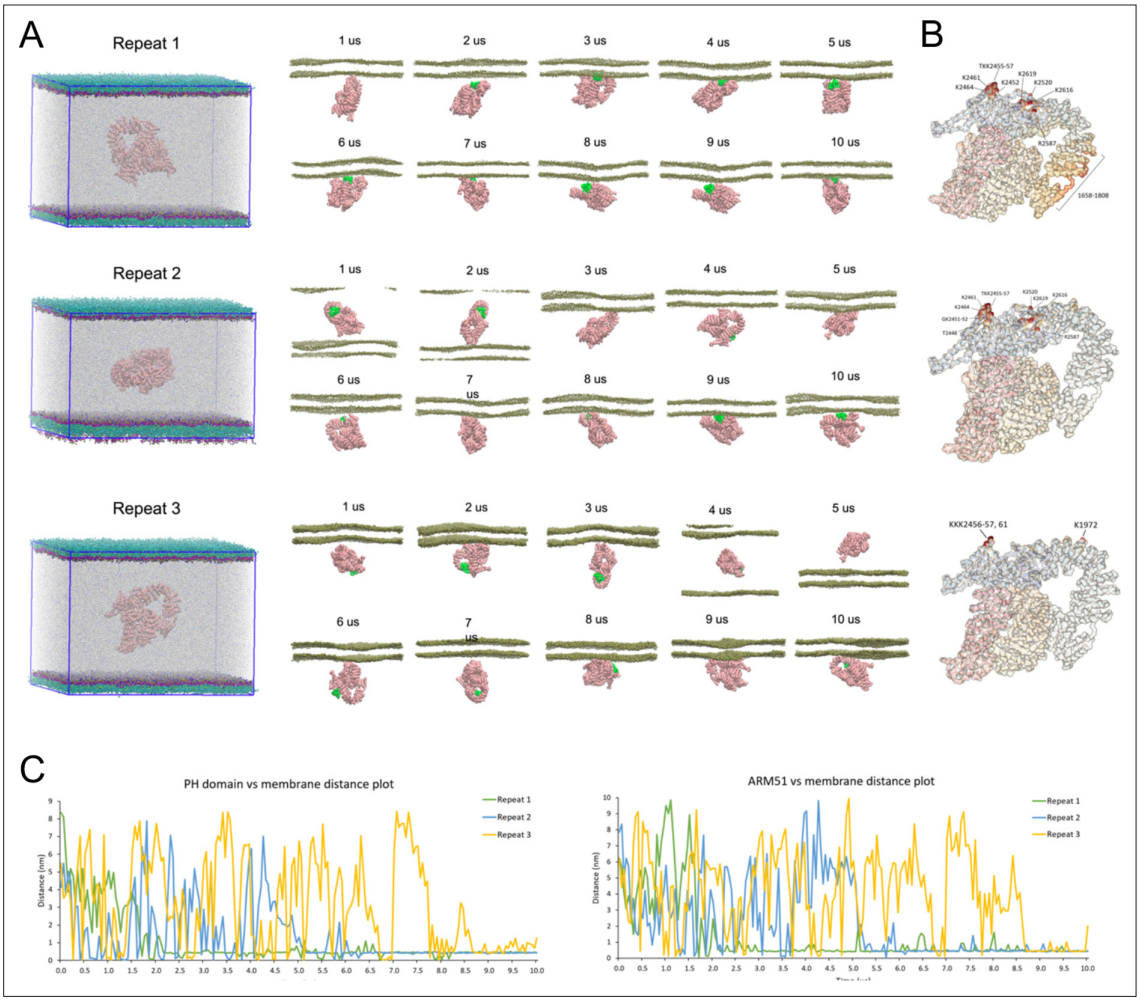

Figure 3—figure supplement 1. Molecular simulations of glideosome-associated connector (GAC) and phosphatidic acid (PA)-containing membranes. (**A**) Binding series and initial orientations for each of three independently generated repeats. The initial configurations show GAC randomly orientated relative to the membrane patch, and the corresponding time series with snapshots at each microsecond are shown. Water is omitted for clarity. (**B**) Lipid contact analysis for the final microsecond of each trajectory. The heatmap and labelled residues show key regions in contact with POPA lipid. (**C**) Centre of mass distance over time for each simulation repeat for the PH domain (left hand panel) and the ARM51 region (right hand panel).

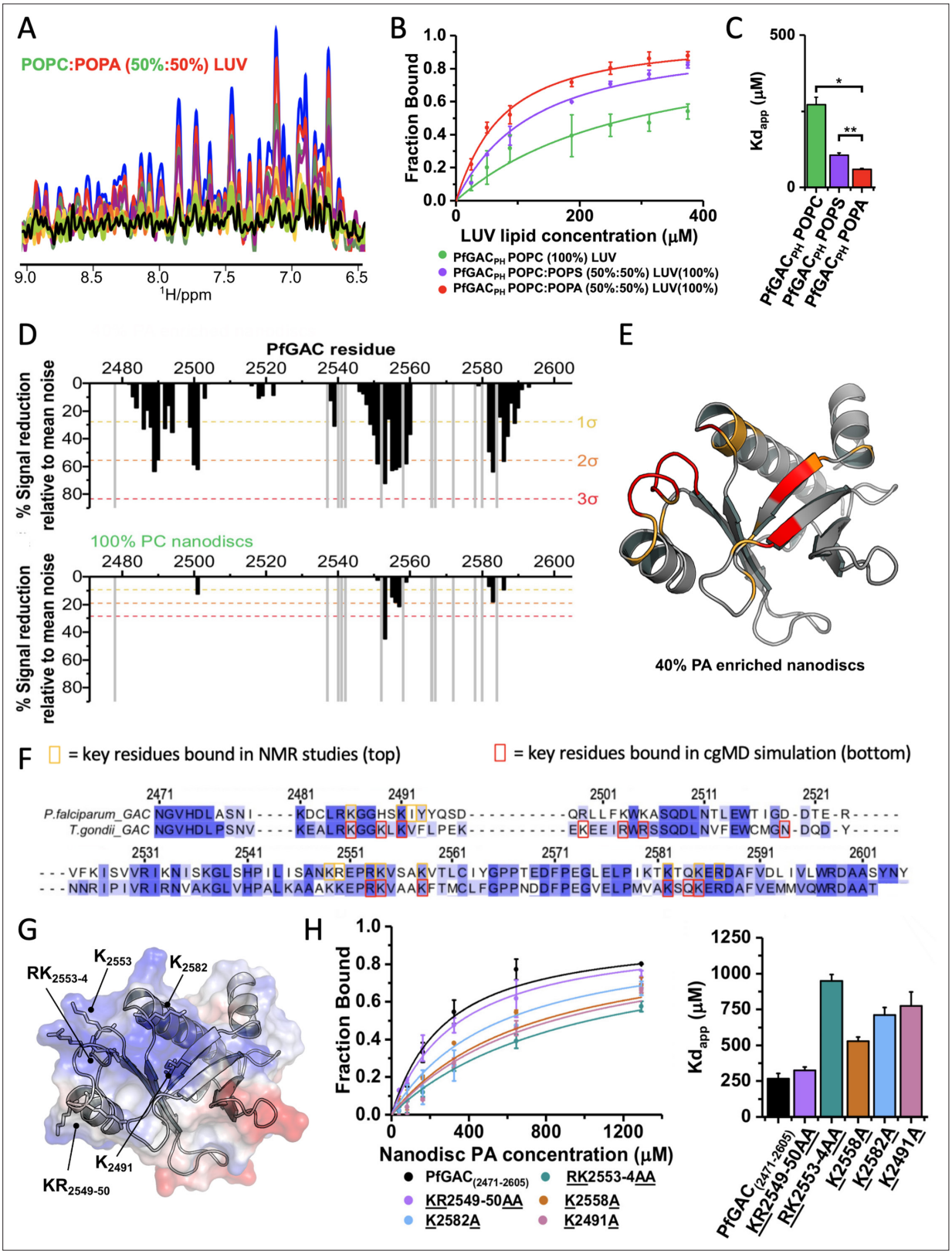

Figure 4. Nuclear magnetic resonance (NMR)-based binding assays for $PfGAC_{2471–2605}$ ($PfGAC_{PH}$) to phosphatidic acid (PA)-enriched unilamellar liposomes. (**A**) 1D 1H-NMR spectrum (9.4–6.5 ppm) of $PfGAC_{PH}$ upon titration with increasing concentrations of large unilamellar vesicles (LUVs) composed of POPC:POPA (50:50%) LUV molar ratios: blue, free $PfGAC_{PH}$ in solution; red 1:2; green 1:4; purple 1:7; yellow 1:15; orange 1:20; lime 1:25; black 1:30. (**B**) Binding curves generated from spectral integration and expressed as the fraction of bound protein for variable LUV compositions

Figure 4 continued on next page

Figure 4 continued

(POPC [100%] green, POPC:POPS [50:50%] purple, or POPC:POPA [50:50%] red). (**C**) Apparent dissociation constants (K_{dapp}) for binding LUVs were calculated from fitting binding curves. (**D**) Plot of $PfGAC_{PH}$ paramagnetic relaxation enhancements (PREs) with PA-enriched MSP1D1H4-5 nanodiscs top (POPC:POPA:PE-DTPA-Gd3+46:40:14%) and bottom (POPC:PE-DTPA-Gd3+86:14%), against sequence number. Dashed lines represent 1 (yellow), 2 (orange), or 3 (red) SD from the mean noise (baseline). (**E**) PA PREs mapped onto the structure of $PfGAC_{PH}$, residues and coloured if greater than 2 (orange) or 3 (red). (**F**) Comparison of contact resides from molecular dynamic (MD) and NMR mapped on to the sequence alignment between $PfGAC_{PH}$ and $TgGAC_{PH}$. (**G**) Electrostatic surface representation of $PfGAC_{PH}$ revealing an extensive surface patch of positive charge surface charge with key mutated residues labelled. (**H**) Binding curves of $PfGAC_{PH}$ mutants generated from 1D NMR titration with calculated Kd_{app}. Data are shown as mean of three replicates ±1σ. Apparent dissociation constants (Kd_{app}) were calculated from fitted binding curves. Data represent mean ±1σ for fitted curves.

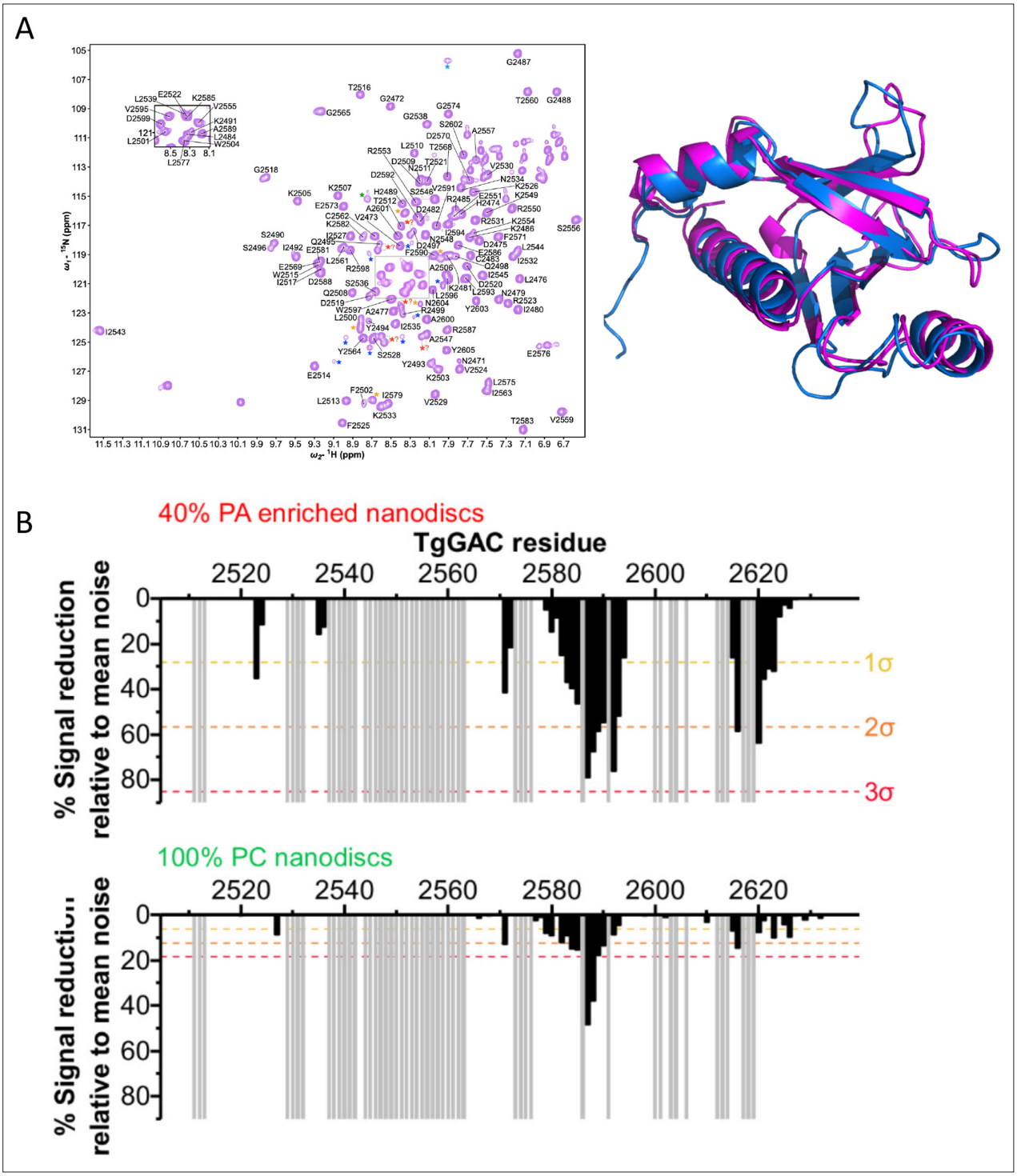

Figure 4—figure supplement 1. Nuclear magnetic resonance (NMR) assignments of $PfGAC_{PH}$ and lipid binding paramagnetic relaxation enhancement (PRE) data for $TgGAC_{PH}$. (**A**) Assigned ^{1}H-^{15}N HSQC for $PfGAC_{PH}$ and comparison of validated structures for $PfGAC_{PH}$ (magenta) and $TgGAC_{PH}$ (blue). (**B**) PRE's with phosphatidic acid (PA)-enriched (top) or phosphatidylcholine (PC) only MSP1D1H4-5 nanodiscs.

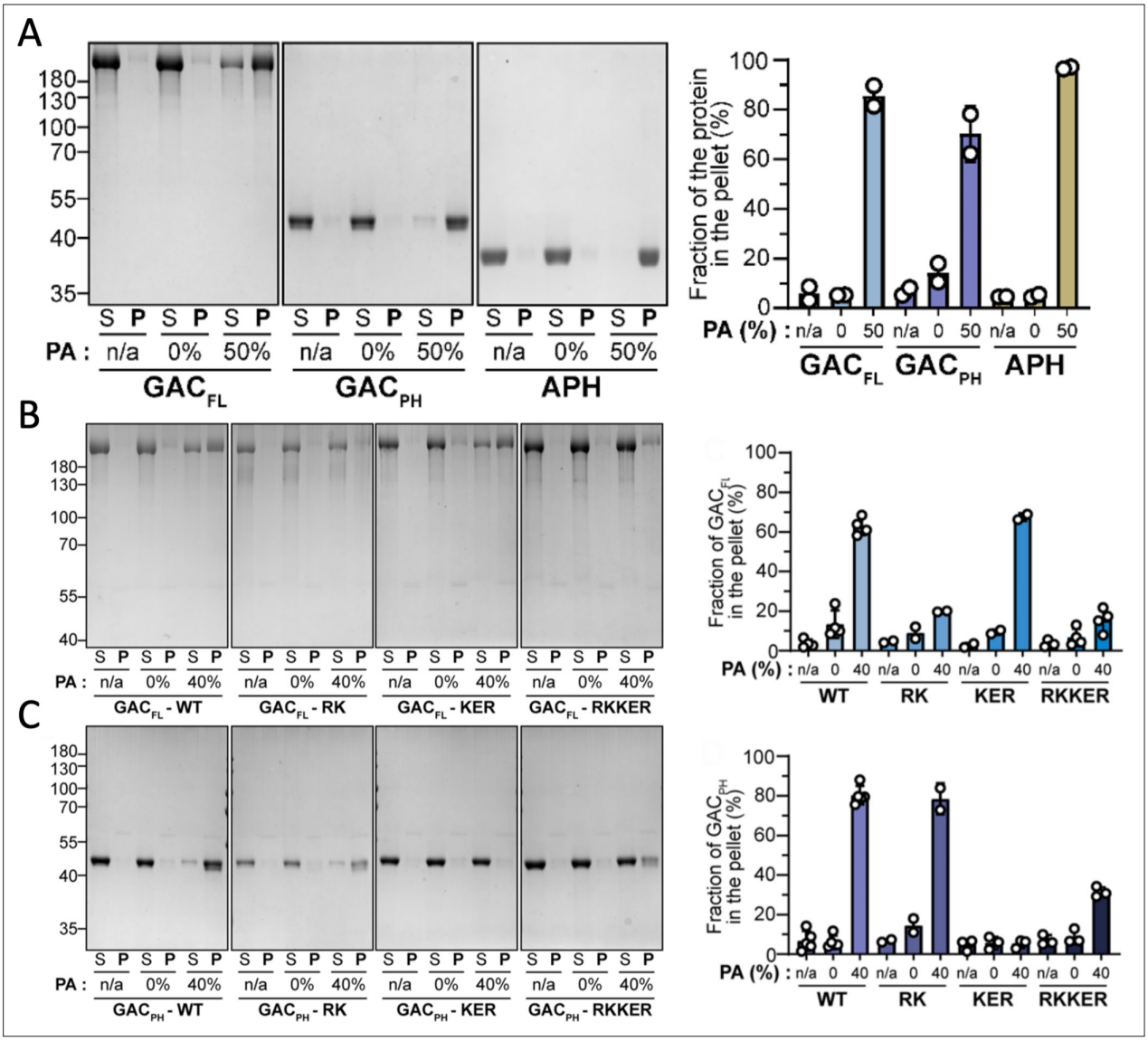

Figure 5. Liposome binding assays of phosphatidic acid (PA) binding by glideosome-associated connector (GAC) and PH domain mutants in vitro. (**A**) Liposome binding assay with the three proteins of interest. A representative gel stained by Coomassie blue (left). Quantification of the pellet fraction measured by band densitometry (n=2). n/a=no liposome. S=supernatant fraction after ultracentrifugation. *P*=pellet fraction after centrifugation (right). (**B**) Representative gel stained by Coomassie blue from liposome binding assays with full-length TgGAC$_{FL}$ and the three mutated versions (left). Quantification of the GAC$_{FL}$ pellet fraction measured by band densitometry (n=2–4; right). n/a=no liposome. S=supernatant fraction after ultracentrifugation. *P*=pellet fraction after centrifugation. RK = RK/AA mutations. KER = KER/AAA mutations. RKKER = RK/AA +KER/AAA mutations. (**C**) Representative gel stained by Coomassie blue from liposome binding assays with TgGAC$_{PH}$ and the three mutated versions (left). Quantification of the GAC$_{PH}$ pellet fraction measured by band densitometry (n=2–4; right).

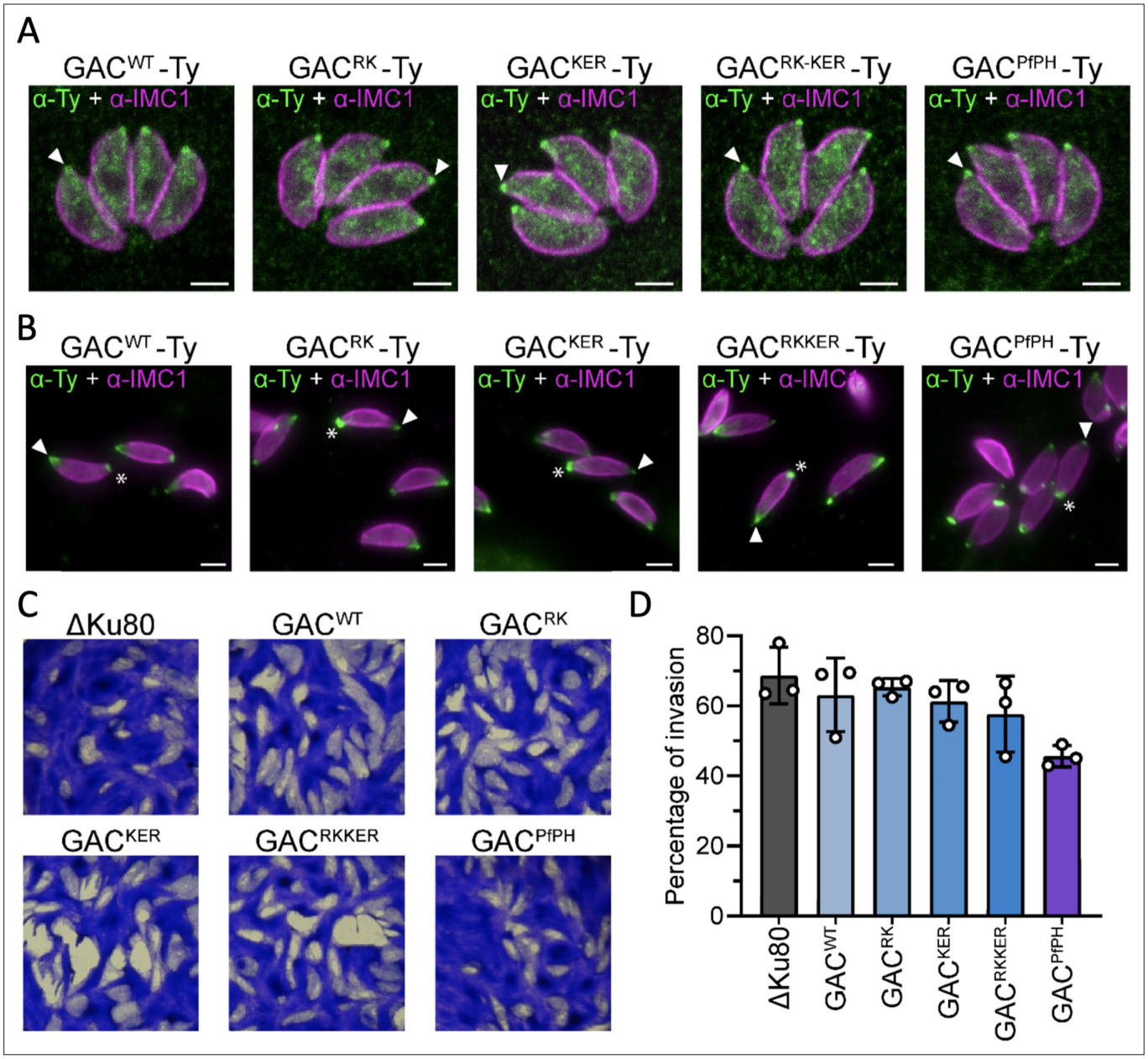

Figure 6. Phenotypical analysis of parasite bearing phosphatidic acid (PA)-binding mutations of glideosome-associated connector (GAC). (**A**) GAC localisation by Immunofluorescence assay (IFA) in intracellular parasites. White arrow = apical pole. Scale bar = 2 µm. (**B**) GAC localisation by IFA in extracellular parasites. White arrow = apical pole. White star = basal pole. Scale bar = 2 µm. (**C**) Plaque assay of the different mutants analysed. (**D**) Red/green invasion assay (n=3). A Δku80 background *T. gondii* strain is used, which is deficient in nonhomologous end joining and provides highly efficient gene replacement.

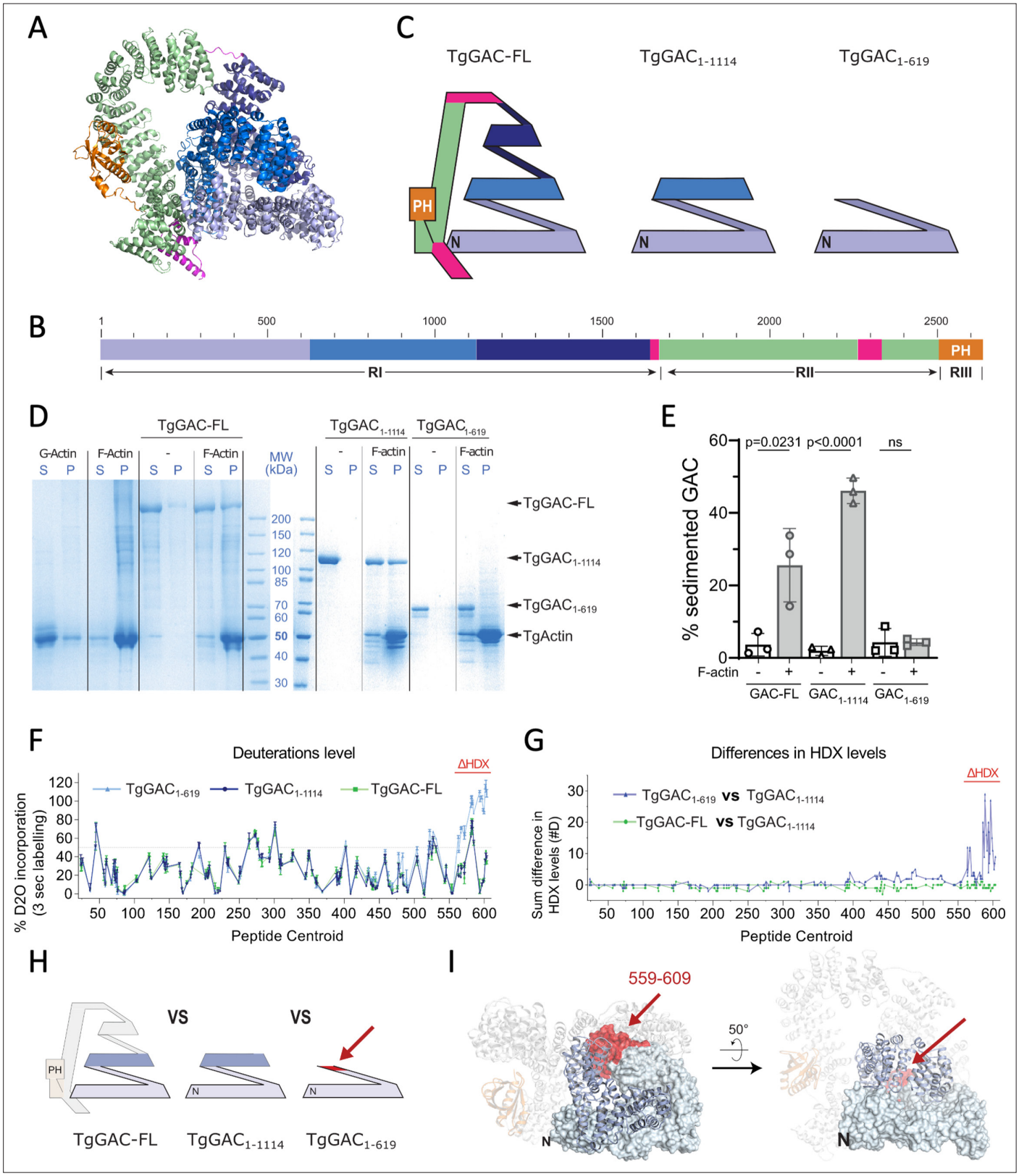

Figure 7. TgGAC interaction with TgActin. (**A**) Cartoon representation of the structure of TgGAC coloured according to schematic representation shown in (**B**). (**C**) Schematic representation of TgGAC structure coloured according to panel (**B**) with illustration of the truncated recombinant TgGAC constructs. (**D**) Coomassie-stained gel analysing proteins remaining in supernatant or sedimenting upon centrifugation at 100,000 g. S: Supernatant. P: Pellet. (**E**) Graphical representation of the percentage of TgGAC co-sedimenting alone or in the presence of TgActin filaments. Data are mean +

Figure 7 continued on next page

Figure 7 continued

SD of three independent experiments. p Value calculated using unpaired t-test. (**F**) Graph displaying deuteration levels for $TgGAC_{1–619}$, $TgGAC_{1–1114}$, and TgGAC-FL. Each dot represents a single peptide where the deuteration level in percentage maximal deuteration is plotted according to the residue number at the centre of the peptide (peptide centroid). (**G**) Comparison of H/D exchange levels for peptides spanning glideosome-associated connector (GAC) residues 1–619 between (i) $TgGAC_{1–619}$ and $TgGAC_{1–1114}$ (blue dots) and between (ii) TgGAC-FL and $TgGAC_{1–1114}$ (green). Each dot represents a peptide with the x-axis indicating peptide centroid as in (**F**). The y-axis indicates the sum of differences in number of deuterons incorporated for each peptide, measured at three deuteration times: 3, 30, and 300 s. Region showing significant differences between $TgGAC_{1–619}$ and $TgGAC_{1–1114}$ is indicated in red. (**H**) Schematic representation of the three GAC constructs studied by hydrogen/deuterium exchange coupled to mass spectrometry (HDX-MS), focussing on the region coloured in light blue (residues 1–619). Red colouring indicates the region where a difference in H/D exchange rate is observed. (**I**) Structure of TgGAC with fragment 1–619 shown as surface representation and highlighted in light blue. Residues 620–1114 are shown in blue, and the remaining of GAC structure is shown in light white. Region displaying a different conformation in $TgGAC_{1–619}$ compared to other TgGAC constructs, with increased H/D exchange rate, is coloured in red.

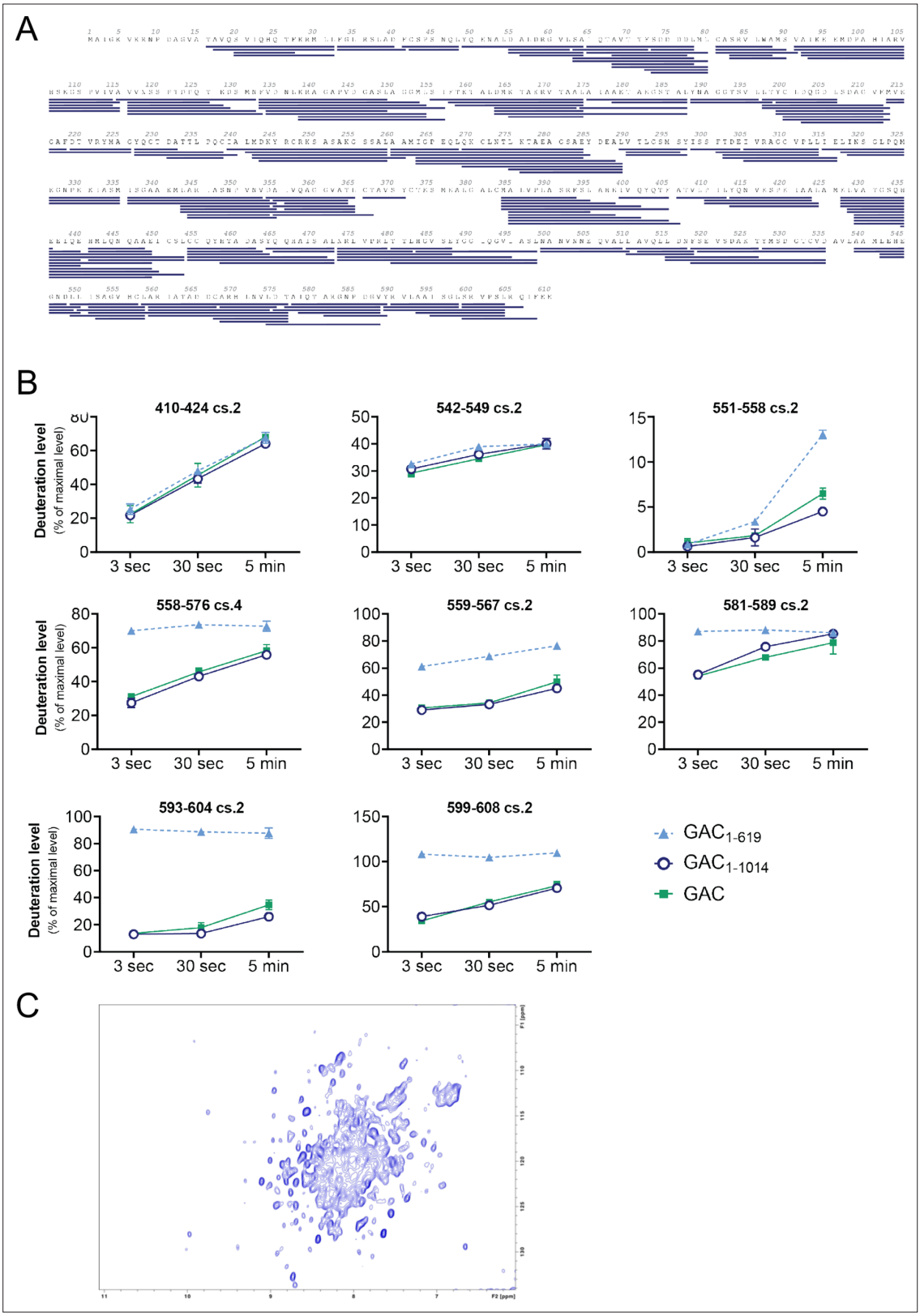

Figure 7—figure supplement 1. Hydrogen/deuterium exchange coupled to mass spectrometry (HDX-MS) and nuclear magnetic resonance (NMR) data for TgGAC$_{1–619}$ construct studied. (**A**) Peptide map showing all peptides analysed in for TgGAC$_{1–619}$. (**B**) Uptake plots for a selection of peptides. (**C**) ^{1}H-^{15}N HSQC NMR spectrum of TgGAC$_{1–619}$ showing a well-folded protein.